Impact parameter dependence of light charged particle production in 25*A* MeV ^{16}O on Tb, Ta, and Au and 35*A* MeV ^{14}N on Sm and Ta

D. Prindle, A. Elmaani, C. Hyde-Wright, W. Jiang, A. A. Sonzogni, and R. Vandenbosch
Nuclear Physics Laboratory, University of Washington, Seattle, Washington 98195

D. Bowman, G. Cron, P. Danielewicz, J. Dinius, W. Hsi, W. G. Lynch, C. Montoya, G. Peaslee, C. Schwarz, M. B. Tsang, and C. Williams
National Superconducting Cyclotron Laboratory, Michigan State University, East Lansing, Michigan 48824

R. T. de Souza, D. Fox, and T. Moore
Indiana University Cyclotron Facility, Indiana University, Bloomington, Indiana 47405

(Received 1 August 1997)

The impact parameter dependence of light charged particle (p,d,t,α) emission has been studied using an impact parameter selection based on coincident detection of residues or fission fragments. The energy spectra at twelve angles between 20° and 150° have been fit by a multiple moving source parametrization. The angle and energy integrated preequilibrium proton multiplicities decrease with increasing impact parameter in qualitative agreement with a Fermi jet calculation. The preequilibrium d/p and t/p multiplicities increase slowly with increasing impact parameter and are nearly identical at the two bombarding energies. The preequilibrium α/p ratio shows a less consistent dependency on impact parameter but decreases significantly with increasing bombardment energy. A calculation of the d/p and t/p multiplicity ratios with a transport model incorporating complex particle emission is quite successful in reproducing the absolute magnitude, impact parameter dependence, and bombarding energy dependence of the experimental total multiplicities. [S0556-2813(98)05203-0]

PACS number(s): 25.70.Jj

I. INTRODUCTION

Particle emission can take place during and after the fusion process in intermediate energy heavy ion reactions. The higher energy particles are typically emitted before the compound nucleus equilibrates and are often referred to as preequilibrium particles. After fusion the excited compound nucleus evaporates particles. If the compound nucleus fissions then each of the fragments can emit particles. All these sources overlap in angle and energy so it is not possible to identify on a particle-by-particle basis which source the particle came from. In practice one decomposes the observed spectra by fitting the data to a moving source parameterization using multiple sources to describe preequilibrium, compound nucleus and fission fragment evaporation sources.

In this report our primary interest is the preequilibrium emission of light charged particles (LCPs). Preequilibrium emission of nucleons (protons and neutrons) has been described quite successfully with a Fermi jet model. In this model the collision process builds a neck between the projectile and target. As particles pass through the neck their Fermi motion is coupled to the projectile velocity and they can pass through the target nucleus, perhaps undergoing a scattering, and emerge with relatively high energy.

Less well understood are the mechanisms contributing to the production of preequilibrium complex light charged particles such as deuterons, tritons and alphas. The shape of the complex particle energy spectra can be related to the proton energy spectrum using a coalescence model, but the absolute multiplicities depend on arbitrary fitting parameters, the coalescence radii. This model also cannot predict the impact parameter dependence of the multiplicities. More recently deuteron [1] and triton [2] formation has been modeled in terms of inverse breakup induced by collisions with nucleons. Incorporation of this mechanism in a thermal transport model allows study of the impact parameter dependence of deuteron and triton formation.

The mechanisms of an intermediate energy heavy ion reaction vary with the impact parameter of the collision. The largest impact parameters lead to quasielastic reactions, with somewhat smaller impact parameters leading to more deeply inelastic collisions. A wide range of impact parameters leads to complete and incomplete fusion (fusionlike) processes. A new tagging technique for defining different mean impact parameter regions within the fusionlike regime has been proposed and used in a previous study [3]. It is based on the angular momentum dependence of evaporation residue-fission competition in the $A=160$–210 region. Low impact parameter (and hence low angular momentum) events lead to evaporation residues, and higher impact parameter (higher angular momentum) events lead to fission fragments. Detection of evaporation residues or fission fragments in a particular event allows tagging on mean impact parameter. The mean impact parameter for a particular type of tag can be adjusted by changing slightly the mass and charge of the target and therefore changing the fissionability of the composite system.

The organization of this paper is as follows. In Sec. II we describe the experiment. We start with a general overview and then describe the fission fragment selection in Sec. II A, the evaporation residue selection in Sec. II B, the LCP selection in Sec. II C and the impact parameter determination in Sec. II D. In Sec. III we discuss the experimental results, starting with the raw multiplicities in Sec. III A, moving

source fits in Sec. III B and comparison of the data to model calculations in Sec. III C. In Sec. IV we summarize the experimental results. Important kinematic correlations arising because of the coincident detection of LCPs and evaporation residues or fission fragments are discussed in Appendix A. We describe the moving source fits in some detail in Appendix B.

II. EXPERIMENT

In this paper we report the results of an experiment performed at the National Superconducting Cyclotron Laboratory at Michigan State University using the Miniball array [4]. The K1200 Cyclotron was used to deliver 25*A* MeV ^{16}O on three targets, ^{159}Tb, ^{181}Ta, and ^{197}Au, respectively 1.5, 1.2, and 1.5 mg/cm^2 thick, and 35*A* MeV ^{14}N on two targets, ^{154}Sm, ^{181}Ta, respectively 0.665 and 1.2 mg/cm^2 thick.

This experiment relied on the detection of fission fragments and evaporation residues in coincidence with LCPs. Each of these particle types was detected in a different detector system which we describe in the next three subsections.

A. Fission fragment selection

Fission fragments were detected in 10 ion chamber detectors [5] covering angles from 16.5° to 160° from the beam and sampling azimuthal angles. Each ion chamber consisted of 3 sections; a gas ionization chamber, a Si surface barrier detector and a CsI scintillation detector. A forward going fission fragment usually reached the Si detector while the backward going fission fragments were often stopped in the gas. In both cases the ionization created by the fission fragments in the gas region was substantial.

The likely backgrounds to fission fragments in the ion chamber detectors were evaporation residues, intermediate mass fragments, and LCPs. The LCPs always created very little ionization in the gas. In principle we could have vetoed them with the CsI(Tl), but in practice a one dimensional cut on the ionization deposition in the gas was very effective. The evaporation residues were apparent only at forward angles. Even though they have a higher charge than do fission fragments, their ionization was smaller because of their lower velocities. Again a one dimensional cut on the ionization deposition in the gas was sufficient to remove these. This leaves the intermediate mass fragments which have a much lower cross section than fission fragments at these energies.

We verify the fission fragment identification by examining the angular distributions. In transforming to the center of mass we assumed an 85% linear momentum transfer for the 25*A* MeV data and 80% for the 35*A* MeV data. This linear momentum transfer was determined by fits to the folding angle distributions [6]. The resulting distributions are reflection symmetric around 90°. The anisotropies vary as expected. The 35*A* MeV ^{14}N data has a lower anisotropy than the 25*A* MeV ^{16}O data, and for a given beam energy the lower mass systems have a larger anisotropy. At a given bombarding energy lower mass targets have higher fission barriers and the angular momentum window contributing to fission has a higher mean square angular momentum value. As the bombarding energy increases the angular momentum does not increase as it has already saturated, whereas the temperature of the system increases diluting the anisotropy.

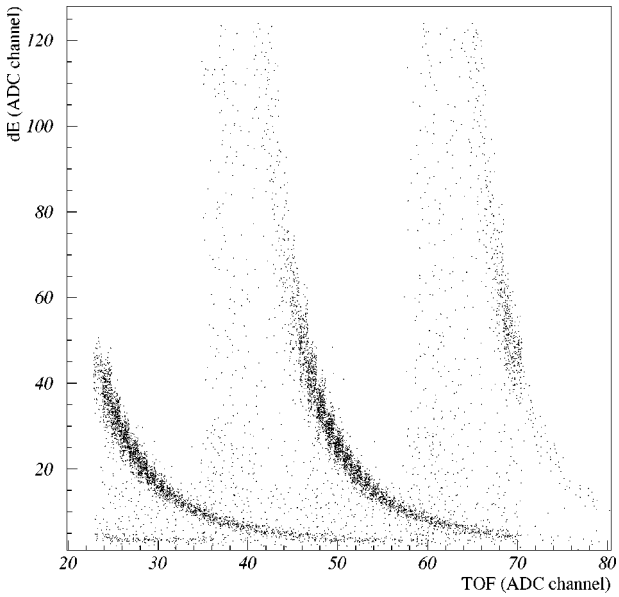

FIG. 1. Energy deposited in the front Si detector versus time of flight for one of the Si telescopes. We have already excluded events in which energy is deposited in the back detector. The TDC start is timed to the beam bunch and the stop is on the energy deposition in the front Si detector. We expect ER energies up to 30 MeV and flight times up to 80 ns.

B. Evaporation residue selection

Evaporation residues were detected in a set of 9 Si telescopes covering angles ranging from 5° to 12° from the beam and distributed uniformly azimuthally. The first element of the telescope (20–400 μm thick) was thick enough to stop all the evaporation residues and gave us an energy and a time signal. The second element (400–1000 μm thick) was used as a veto detector. The evaporation residues were identified through their distinctive signature in a two dimensional plot of energy versus time of flight.

The evaporation residue trigger required a signal in the front Si detector and no signal in the back detector of the telescope. In Fig. 1 we show the deposited energy versus the time of flight for one of the telescopes after applying the veto. There are two time bands. This is because the time between bunches (79 ns for the 35*A* MeV ^{14}N beam, 93 ns for the 25*A* MeV ^{16}O beam) was less than the maximum evaporation residue flight time so a fast trigger from the miniball could come one time bunch early. Thus we made the evaporation residue trigger coincidence two beam bunches wide. In the data analysis we further required the signal to fall within a gate drawn in the two-dimensional time of flight versus *E* scatter plot. This rejected a small contamination due to light particles that were not vetoed.

C. Light charged particle selection

The LCPs were detected and identified by the miniball array [4]. This array consists of rings of phoswich detectors, each detector consisting of a thin fast plastic in front of a CsI

TABLE I. Measured cross sections and deduced mean impact parameters.

		25*A* MeV ^{16}O		
Target	σ_{ER}(mb)	$\langle b_{ER}\rangle$(fm)	σ_{FF}(mb)	$\langle b_{FF}\rangle$(fm)
Tb	1020	3.75	700	6.87
Ta	410	2.47	1290	6.06
Au	169	1.66		
		35*A* MeV ^{14}N		
Target	σ_{ER}(mb)	$\langle b_{ER}\rangle$(fm)	σ_{FF}(mb)	$\langle b_{FF}\rangle$(fm)
Sm	1380	4.20	96	6.30
Ta	780	3.37	673	5.74

crystal. The miniball array covered the angles from 16.5° to 160° from the beam and all angles in azimuth. Some of the detectors were replaced by ion chamber detectors (one per ring). The solid angle useful for LCP dectection in this experement was 65% of 4π. The CsI pulse shape depends on particle type. We collect charge during a gate extending from 400 ns to 800 ns after the start of the signal (slow gate) and also during a gate from 1 μs to 2 μs (tail gate). The $p,d,t,$ and α were selected by using a 2D gate in this slow versus tail space. Above about 40 MeV we can separate ^{3}He from ^{4}He. Since we cannot distinguish ^{3}He from ^{4}He at lower energies we add them together and treat them as ^{4}He in the analysis. In the reactions studied here the ^{3}He yield is less than 1/5 of the ^{4}He yield in the energy region where they could be separated.

The miniball energy response was calibrated using a set of runs with mixed ^{2}H and ^{4}He particles elastically scattered from a Au target and also ^{12}C particles on a CH_2 target. All calibration beams were obtained at 22*A* MeV. Different energies of the mixed beam were obtained by passing it through an Al degrader 0.072 inches thick rotated to various angles before scattering off the Au target. A typical counter ended up with five proton calibration points ranging from 35 MeV to 75 MeV, nine deuteron calibration points ranging from near threshold to 44 MeV and four alpha calibration points ranging from 20 MeV to 88 MeV.

The elastic scattering used for the energy calibration only gave us data at forward angles. We moved most of the backward detectors to forward positions and repeated the calibration runs. A few of the counters ended up with no calibration data. We determined the calibration constants for these counters by forcing their proton spectra to agree with adjacent counters that were calibrated.

The energy calibration should be accurate to within 2 to 3 MeV over the range covered by the calibration points.

D. Impact parameter determination

The mean impact parameters for the evaporation residue and fission fragment tags have been deduced in the sharp cutoff approximation from fission and evaporation residue cross sections measured as part of this study. The procedures used and some cross sections at 35*A* MeV have been reported previously [6]. The measured cross sections and deduced impact parameters are summarized in Table I.

The Au fission fragment data sample is expected to have a large contribution due to deep inelastic scattering, so we have omitted that data set from this paper. The uncertainties in the absolute cross sections are 10 to 20%, leading to uncertainties in the mean impact parameter of 5 to 10%.

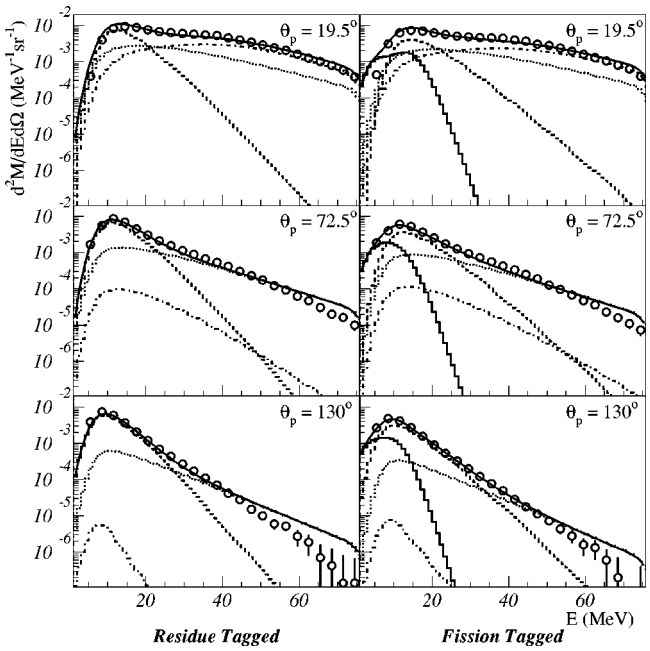

FIG. 2. Proton energy spectra for 25*A* MeV ^{16}O on Ta at representative angles as listed in each panel. The three panels on the left are protons in coincidence with evaporation residues and the three panels on the right are protons in coincidence with fission fragments. The data are the open circles. The solid line is the sum of the moving source fit components. The dot-dashed line is the projectilelike source, the dotted line is the prompt source, and the dashed line is the compound nucleus source. Evaporation from the fission fragments is the solid histogram at low energies in the right panels.

III. LIGHT CHARGED PARTICLE CHARACTERIZATION

Samples of LCP energy spectra are shown in Figs. 2 and 3. These figures show proton and alpha spectra at representative angles for the 25*A* MeV ^{16}O on Ta data samples. There is a low energy peak which is due to particle evaporation from the compound nucleus and this component has only a weak dependence on angle. The high energy component of the spectra, due to preequilibrium emission, drops off rather quickly with increasing angle. This is especially true for α particles. The moving source parameterization of these spectra is discussed in Sec. III B 1.

A. Raw multiplicities

The raw multiplicities are the number of LCPs observed divided by the total number of events in the sample after correcting for the solid angle (assuming isotropy) by scaling up by 1/0.65. Raw multiplicities are affected by nonisotropic angular distributions and energy thresholds. Since the miniball covers a large solid angle and measures LCP energies over most of the region kinematically allowed in this experiment, the raw multiplicities are a reasonable measure of the total multiplicity.

The raw multiplicities of evaporation residue and fission fragment samples for the 25*A* MeV and 35*A* MeV data are

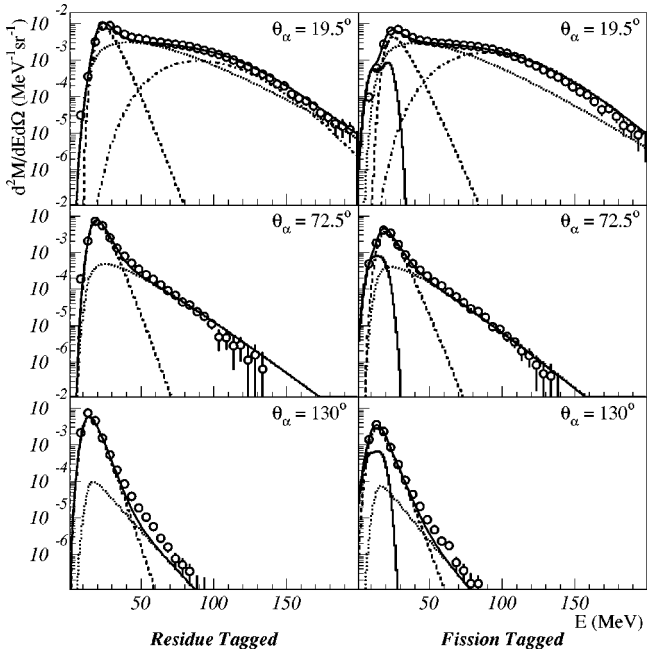

FIG. 3. α particle energy spectra for 25A MeV ^{16}O on Ta at representative angles as listed in each panel. The three panels on the left are α particles in coincidence with evaporation residues and the three panels on the right are α particles in coincidence with fission fragments. The data are the open circles. The solid line is the sum of the moving source fit components. The dot-dashed line is the projectilelike source, the dotted line is the prompt source, and the dashed line is the compound nucleus source. Evaporation from the fission fragments is the solid histogram at low energies in the right panels.

listed in Tables II and III. Proton and alpha multiplicities are roughly equal, with deuteron multiplicities about a factor of three smaller and triton multiplicities another factor of two smaller.

Another way to determine the average multiplicity is to fit the distribution of multiplicities. Assuming all particles are detected independently with a fixed efficiency, ϵ, we can infer the emitted distribution of multiplicities from the observed distribution. The probability of detecting k particles when there were N emitted is given by the binomial distribution:

$$p_k = \binom{N}{k} \epsilon^k (\epsilon - 1)^{N-k}. \tag{1}$$

In an event for which we detected k particles the actual number of particles emitted may be any number higher than or

TABLE II. Raw multiplicities for LCP in coincidence with evaporation residues or fission fragments for the 25A MeV ^{16}O data. Statistical errors are typically less than 10^{-3}. We have corrected for solid angle assuming 65% coverage.

LCP	Au ER	Ta ER	Tb ER	Ta FF	Tb FF
Proton	1.677	1.796	1.991	1.252	1.436
Deuteron	0.541	0.561	0.580	0.429	0.449
Triton	0.265	0.280	0.260	0.231	0.208
He	1.919	1.605	1.509	1.019	1.051

TABLE III. Raw multiplicities for LCPs in coincidence with evaporation residues or fission fragments for the 35A MeV data ^{14}N. Statistical errors are about 2×10^{-3} for the evaporation residue data and 5×10^{-3} for the fission fragment data. We have corrected for solid angle assuming 65% coverage.

LCP	Ta ER	Sm ER	Ta FF	Sm FF
Proton	2.168	2.133	1.605	1.643
Deuteron	0.740	0.757	0.614	0.630
Triton	0.388	0.387	0.343	0.329
He	1.633	1.445	1.135	1.230

equal to k. Thus for a set of events in which we detected k particles n times the relationship between the observed, n, and emitted, N, numbers of particles is

$$n_k = \sum_{i=k}^{m} \binom{i}{k} \epsilon^k (\epsilon - 1)^{i-k} N_i \tag{2}$$

where m is large enough that $N_m \leqslant 1$. The actual and observed distributions are related by an upper triagonal matrix which allows us to solve for N by back-substitution. A more detailed treatment of this subject can be found in [7].

If the LCPs are emitted independently we expect the emitted multiplicities to follow a Poisson distribution. In Fig. 4 we show an example of Poisson fits to the 25A MeV ^{16}O on Ta target data, after the observed particle distributions have been corrected for solid angle. The mean determined by the Poisson fit is typically within 1% of the raw multiplicity listed in Table II. The fits are reasonable, although the Poisson distribution is slightly broader than the data. If the data are constrained by a conservation law, such as energy conservation, the multiplicity distribution will be narrowed [8].

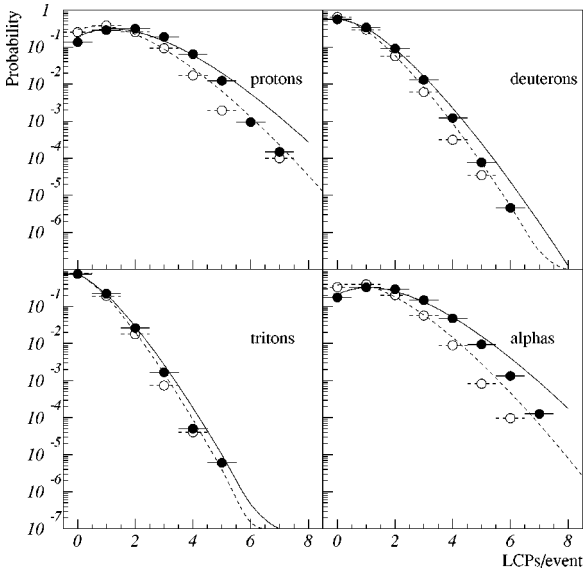

FIG. 4. Probability functions of LCPs. The data are the circles, filled for evaporation residue coincident, hollow for fission fragment coincident. The curves are Poisson distribution fits to the evaporation residue coincident data. The data have been corrected for solid angle acceptance as described in the text.

The data being narrower than the Poisson distribution is an indication that the LCPs are not emitted completely independently.

It is interesting that in every case the multiplicity of LCPs in coincidence with evaporation residues is larger than the the multiplicity of LCPs in coincidence with fission fragments. The larger evaporation residue tagged multiplicity has been observed in other systems [9]. This ''excess'' multiplicity is concentrated in low energy particles, which can be seen by comparing evaporation residue coincident α particles with fission fragment coincident α particles as plotted in Fig. 3. For backward angles, which is almost completely evaporative from the compound nucleus, the yield of α particles in coincidence with evaporation residues is roughly twice the yield of α particles in coincidence with fission fragments. This is an indication that fission occurs before the compound nucleus exhausts its energy in LCP evaporation. Presumably the fission fragments evaporate a larger fraction of their excitation energy in neutrons since they are more neutron rich than the compound nucleus. The data at forward angles has a low energy peak due to evaporation from the compound nucleus and a high energy component from prompt emission. The yield of prompt particles is very similar for the two tags. Studies of particle-particle correlations in similar systems [10] indicate that the most energetic LCPs are emitted within a few tens of fm/c while the least energetic LCPs have emission times of thousands of fm/c. Fission occurring after hundreds of fm/c is consistent with these observations. The implications of fission occurring before the LCP evaporation chain is completed are discussed more in Sec. III B 1.

B. Moving source fits

A standard way to describe the LCP spectra and their angular dependence is to assume particle emission from a thermal source moving with some velocity in the laboratory [11,12]. A thermal source is described by a temperature, T_{source}, and multiplicity, M_{source}. The source velocity, v_{source}, is a third parameter and since the LCPs are charged the Coulomb barrier, V_{source}, is a fourth parameter.

For beam energies lower than about 10A MeV it is sufficient to use a single equilibrium source with v_{equil} fixed at the compound nucleus velocity. When the compound nucleus fissions each of the fragments evaporates LCPs from its surface with v_{FF} equal to the fragment velocities. For beam energies above about 10A MeV it is necessary to introduce a ''prompt'' source with v_{prompt} near one half the beam velocity. This source is usually taken to be a volume source. We find that at 25A MeV and 35A MeV we need to introduce an additional ''projectilelike'' source with v_{proj} near the beam velocity. We fix v_{proj} at 90% of the beam velocity. We attribute the need for this source to the emission of particles from the projectile early in its stopping process.

We should emphasize that while thermal moving source parameterizations of LCP emissions give a reasonably accurate description of the angular and energy distributions of the LCPs in terms of parameters which are easily understood, they are of course not a rigorous description. A microscopic description of the physics will not factor into these few sources with discrete velocities. Another note of caution in the comparison of the fitted parameters is that there are correlations between the different sources.

Although moving source fits are a standard analysis technique there are a number of variations on how they are done and this makes it difficult to compare results of different experiments. In Appendix B we describe in detail how we do the moving source fits.

1. Results of moving source fits

Samples of moving source fits are shown superposed on the data in Figs. 2 and 3. The fits do a reasonable job of reproducing the data. At the most forward angle the high energy LCPs are dominated by the projectilelike component, but this drops off in angle very quickly compared to the prompt source. This angular dependence of the projectilelike component is especially noticeable for α particles which have a stronger kinematic focusing because of their larger mass. At far backward angles the prompt source is very small compared to the compound nucleus source whose emission is nearly isotropic. The fission fragment evaporative source is only important for the low energy LCPs. While the fission fragment contribution to the proton and alpha spectra is significant, there is no clear signal that evaporation from the fission fragments contributes to the deuteron and triton spectra.

The fit parameters are listed in Tables IV and V. The χ^2_ν values are not 1.0, but depend on the statistics, indicating that the moving source parametrization is not a perfect description of the data. This is to be expected as we have replaced a continuum of source velocities with three discrete source velocities. However the parameters follow the expected trends, and where we can compare to other experiments we get similar results, indicating this is a useful parameterization.

The Coulomb barrier, V_{equil} is around 6 MeV for p, d, and t and 12 MeV for α emission. Heavier systems, which have more charge, have a higher V_{equil}. Somewhat unexpected is that V_{equil} is appreciably lower than one would calculate for the Coulomb energy of touching spheres, where one sphere is the compound nucleus and the other sphere is the LCP. Low Coulomb barriers for particle emission from the compound nucleus have been observed in other experiments [9,13]. V_{FF} is closer to the calculated values for touching spheres than is V_{equil}, but is still low.

The prompt source velocities are between 40% and 50% of the beam velocity, consistent with other findings [12,14]. Using the prompt and projectilelike source velocities and multiplicities listed in Table IV we calculate that the preequilibrium LCPs carry 10 to 15% of the beam momentum for the 25A MeV ^{16}O and 15 to 20% of the beam momentum for the 35A MeV ^{14}N. Assuming the rest of the beam momentum goes into the compound nucleus velocity we find the evaporation residue and fission fragment events have very similar linear momentum transfer and we have good agreement with a folding angle analysis of the fission fragments [6]. We estimate $v_{\text{equil}}/v_{\text{beam}}$ should be 0.07 for the 25A MeV ^{16}O on Ta data and 0.06 for the 35A MeV ^{14}N on Ta data with an inverse dependence on the target mass. The fitted evaporative source velocities are all quite consistent with these values and show the correct target mass dependence.

TABLE IV. Moving source fit parameters for preequilibrium components. Statistical errors (enclosed in parentheses) are omitted when smaller than the least significant digit.

LCP	Beam	Tag	Target	χ_ν	M_{proj}	T_{proj}	M_{prompt}	T_{prompt}	v_{prompt}/v_b
proton	25*A* MeV ^{16}O	ER	Au	2.16	0.158	3.93(4)	0.384	10.67(7)	0.38(1)
			Ta	8.21	0.175	4.65(2)	0.420	10.78(3)	0.38
			Tb	11.94	0.187	5.23(2)	0.469	10.40(2)	0.36
		FF	Ta	5.52	0.160	5.25(2)	0.312	10.85(3)	0.47
			Tb	2.06	0.156	5.63(5)	0.279	10.75(8)	0.46(1)
	35*A* MeV ^{14}N	ER	Ta	4.54	0.248	6.50(5)	0.592	13.60(7)	0.32
			Sm	6.01	0.288	7.04(3)	0.590	12.84(5)	0.30
		FF	Ta	1.95	0.269(1)	7.02(9)	0.536(1)	13.74(13)	0.41(1)
			Sm	1.07	0.211(2)	7.35(33)	0.458(3)	13.32(47)	0.48(4)
deuteron	25*A* MeV ^{16}O	ER	Au	1.52	0.042	3.66(10)	0.165	11.44(7)	0.50(1)
			Ta	4.49	0.062	4.53(4)	0.199	12.11(3)	0.46
			Tb	6.29	0.069	5.30(3)	0.226	12.39(2)	0.43
		FF	Ta	3.66	0.068	5.63(4)	0.195	12.52(3)	0.45
			Tb	1.51	0.064	6.15(9)	0.190	12.29(6)	0.42
	35*A* MeV ^{14}N	ER	Ta	2.46	0.122	7.88(9)	0.268	15.92(7)	0.39
			Sm	3.44	0.154	8.79(7)	0.274	15.34(6)	0.37
		FF	Ta	1.39	0.167	9.23(15)	0.281	15.89(13)	0.40(1)
			Sm	0.98	0.100(2)	9.53(72)	0.261(1)	16.04(41)	0.48(3)
triton	25*A* MeV ^{16}O	ER	Au	1.37	0.014	3.53(20)	0.143	10.25(5)	0.39
			Ta	4.06	0.022	4.46(7)	0.159	10.93(2)	0.41
			Tb	4.98	0.023	4.95(7)	0.163	11.61(2)	0.41
		FF	Ta	3.71	0.031	5.17(7)	0.153	11.99(2)	0.42
			Tb	1.51	0.028	6.46(14)	0.142	11.38(5)	0.37
	35*A* MeV ^{14}N	ER	Ta	2.22	0.063	9.91(21)	0.182	15.35(7)	0.36
			Sm	3.02	0.076	10.44(15)	0.185	14.27(5)	0.39
		FF	Ta	1.36	0.112	12.10(23)	0.195	14.13(10)	0.35
			Sm	0.87	0.112(1)	12.73(57)	0.209(1)	12.47(32)	0.26(1)
alpha	25*A* MeV ^{16}O	ER	Au	1.51	0.055	3.54(10)	0.414	12.11(4)	0.43
			Ta	4.74	0.073	3.69(4)	0.394	12.80(2)	0.43
			Tb	5.65	0.074	4.10(3)	0.412	13.22(2)	0.43
		FF	Ta	2.15	0.121	4.20(2)	0.353	12.00(2)	0.44
			Tb	0.97	0.075	4.57(6)	0.305	12.00(4)	0.43
	35*A* MeV ^{14}N	ER	Ta	2.12	0.082	8.15(10)	0.353	17.36(5)	0.41
			Sm	2.57	0.121	9.04(7)	0.350	16.44(4)	0.41
		FF	Ta	0.97	0.125	8.77(11)	0.350	16.11(7)	0.42
			Sm	0.59	0.095	15.68(53)	0.325(1)	16.88(27)	0.38(1)

The source temperatures are $T_{\text{proj}} \approx 4$ MeV, $T_{\text{prompt}} \approx 11$ MeV, and $T_{\text{equil}} \approx 4$ MeV for the 25*A* MeV ^{16}O data and $T_{\text{proj}} \approx 8$ MeV, $T_{\text{prompt}} \approx 14$ MeV, and $T_{\text{equil}} \approx 4.5$ MeV for the 35*A* MeV ^{14}N data. Other experiments using three source fits find similar temperatures when fitting to LCP [12,14] and neutron [15] distributions. One expects that $T_{\text{equil}}(t) > T_{\text{equil}}(d) > T_{\text{equil}}(p)$ due to the heavier particles being emitted earlier. This trend is observed for the evaporation residue coincident data. The fission fragment coincident T_{equil} are higher than the evaporation residue coincident T_{equil}, consistent with fission terminating the evaporation chain. T_{equil} has a very weak dependence on beam energy which is expected since the energy deposition only increases slowly with increasing bombarding energy as a larger fraction of the bombarding energy goes into preequilibrium emission. Since the prompt and projectilelike sources represent nonequilibrium processes the temperatures associated with these sources should be considered phenomenological rather than the temperature of a thermally equilibrated system. T_{prompt} shows no target dependence and a weak dependence on the beam energy. T_{proj} does show a target dependence, the more peripheral collisions exhibiting a higher projectilelike temperature. T_{proj} also shows a dependence on beam energy.

We are primarily interested in the preequilibrium multiplicities. For protons and alphas the equilibrium source is dominant. For deuterons the equilibrium and prompt sources have roughly equal multiplicities and for tritons the prompt source is the largest one. The equilibrium multiplicities of protons and alphas in coincidence with evaporation residues are about two times the multiplicities in coincidence with fission fragments, indicating that fission occurs before the

TABLE V. Moving source fit parameters for equilibrium components. Statistical errors (enclosed in parentheses) are omitted when smaller than the least significant digit.

LCP	Beam	Tag	Target	$M_{\rm equil}$	$T_{\rm equil}$	$v_{\rm equil}/v_b$	$V_{\rm equil}$	$M_{\rm FF}$	$T_{\rm FF}$	$V_{\rm FF}$
proton	^{16}O	ER	Au	0.835	3.57(2)	0.07	6.36(2)			
			Ta	0.893	3.43(1)	0.07	5.70(1)			
			Tb	1.054	3.18(1)	0.07	4.90(1)			
		FF	Ta	0.561	4.15(1)	0.09	6.34(2)	0.110	1.03(3)	5.16(5)
			Tb	0.633(1)	4.22(3)	0.10	5.42(6)	0.163	1.33(6)	3.81(7)
	^{14}N	ER	Ta	0.922	3.64(2)	0.04	5.59(1)			
			Sm	0.852	3.35(1)	0.05	4.76(1)			
		FF	Ta	0.542(1)	4.73(6)	0.05	5.99(9)	0.155(1)	1.50(10)	5.54(14)
			Sm	0.545(6)	6.42(24)	0.06	4.46(59)	0.244(3)	1.62(22)	4.13(34)
deuteron	^{16}O	ER	Au	0.262	5.04(3)	0.09	5.78(3)			
			Ta	0.233	4.03(1)	0.08	6.28(1)			
			Tb	0.242	3.72(1)	0.08	5.93(1)			
		FF	Ta	0.197	3.73(1)	0.08	6.29(1)	0.001	0.79(20)	7.34(24)
			Tb	0.196	3.67(3)	0.08	5.89(3)	0.003	0.10(49)	6.32(57)
	^{14}N	ER	Ta	0.260	4.11(2)	0.06	6.28(2)			
			Sm	0.239	3.63(2)	0.06	5.98(2)			
		FF	Ta	0.234	3.98(4)	0.06	6.21(4)	0.000	0.01(3)	7.58(15)
			Sm	0.368(1)	5.32(14)	0.08	4.78(13)	0.009(1)	0.73(**)	7.22(**)
triton	^{16}O	ER	Au	0.074	4.17(4)	0.06	8.60(3)			
			Ta	0.072	4.44(2)	0.07	8.26(2)			
			Tb	0.067	4.61(2)	0.07	7.53(1)			
		FF	Ta	0.057	4.71(5)	0.08	7.86(1)	0.002	1.90(36)	14.51(54)
			Tb	0.036	3.72(17)	0.07	7.98(6)	0.003	3.15(66)	8.77(71)
	^{14}N	ER	Ta	0.118	4.93(3)	0.04	8.37(2)			
			Sm	0.108	5.24(3)	0.05	7.86(2)			
		FF	Ta	0.092	4.23(13)	0.04	8.54(4)	0.000	2.28(**)	17.20(**)
			Sm	0.066(1)	3.94(28)	0.05	8.24(14)	0.019	43.44(**)	5.33(**)
alpha	^{16}O	ER	Au	1.272	3.68(1)	0.07	13.57(2)			
			Ta	1.042	3.59(1)	0.07	12.82(1)			
			Tb	1.007	3.52	0.08	11.56(1)			
		FF	Ta	0.575	3.98(1)	0.09	12.51(1)	0.065	0.32(1)	12.25(1)
			Tb	0.565	4.07(2)	0.10	10.95(3)	0.089	1.41(10)	8.76(17)
	^{14}N	ER	Ta	1.019	4.03(1)	0.06	12.37(2)			
			Sm	0.839	3.89(1)	0.06	10.85(1)			
		FF	Ta	0.624(1)	4.41(4)	0.08	11.42(5)	0.083	2.42(19)	10.44(32)
			Sm	0.562(3)	4.95(17)	0.08	9.38(21)	0.151(2)	3.36(39)	7.06(76)

particle evaporation chain is done. Subtracting the energy going into the production of prompt LCPs leaves these systems with from 260 to 340 MeV of excitation energy. Assuming fission occurs when the system drops to 100 MeV of excitation energy and that each evaporated particle takes away a fixed amount of energy we expect that the ratio of evaporation residue coincident to fission fragment coincident equilibrium multiplicities will be about 1.5 for the 35A MeV systems and around 1.8 for the 25A MeV systems. The proton and alpha equilibrium multiplicity ratios are reasonably close to these values. After fission the fragments should share the rest of the excitation energy so one might expect the LCP emission from the fragments would make up for the fission fragment equilibrium multiplicity deficit, however these fragments are neutron rich so most of this excitation energy actually goes into neutron production. We do see a clear indication of proton and alpha evaporation from the fragments, but the multiplicity of deuteron and triton evaporation from the fragments is at least 30 times smaller than that of the protons.

The preequilibrium multiplicities are plotted in Fig. 5. Panel (a) of this figure shows the proton preequilibrium multiplicities and panels (b), (c), and (d) show the ratios of the d, t, and α to the p preequilibrium multiplicities. We normalize to the proton preequilibrium multiplicities in order to minimize possible systematic errors due to the different kinematic corrections of the fission fragment and evaporation residue tags. We see a possible discontinuity in the 25A MeV proton multiplicities when going from the fission fragment tag to the evaporation residue tag. The prompt deuteron to proton and triton to proton ratios are rather smooth, showing a small decrease for more central impacts. This behavior is very similar to that observed in our earlier work at 14A MeV [3]. Interestingly the 25A MeV and the

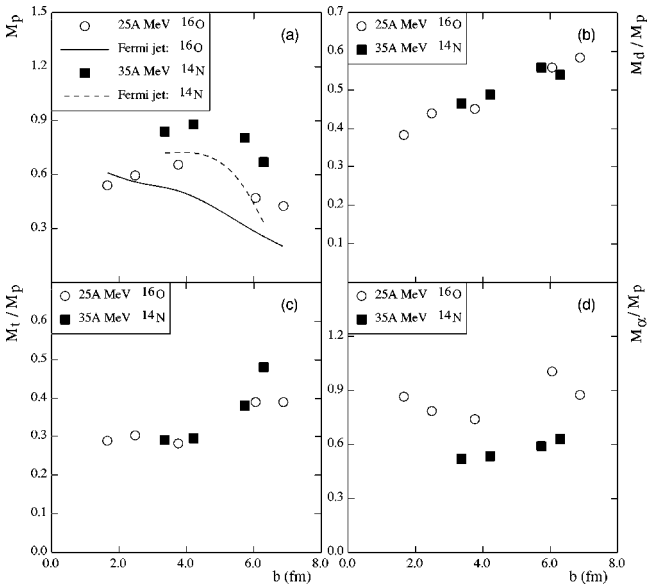

FIG. 5. Preequilibrium p multiplicity [in panel (a)] and the ratios of d, t, and α to p preequilibrium multiplicities [in panels (b), (c), and (d)] as a function of mean impact parameter. The 25A MeV ^{16}O data are the circles, 35A MeV ^{14}N data are the squares. The preequilibrium multiplicities are the sum of the projectilelike and prompt sources, taken from Table IV. The full and dashed curves are for preequilibrium protons originating in the projectile as calculated by a Fermi jet model described in Sec. III C 1. The mean impact parameter values are deduced from the evaporation residue and fission fragment cross sections as listed in Table I. Mean b values less than 5 fm are associated with evaporation residues and those with values greater than 5 fm with fission fragments.

35A MeV ratios seem to fall on the same curve. The common d/p and t/p ratios at 25A MeV and 35A MeV are however greater than at 14A MeV, indicating a saturation in the ratio by 25A MeV. The prompt α/p ratios do not follow a smooth trend, showing a discontinuity when going from the evaporation residue to the fission fragment tag. This behavior was also observed at 14A MeV. It is also interesting to note that the α/p ratio decreases monotonically with energy, in contrast to the behavior of the d/p and t/p ratios. This suggests the contribution of a somewhat different formation mechanism for the α particles as compared to the lighter complex particles.

Another interesting aspect of this work is the possibility to test another popular technique for impact parameter selection. It is often assumed that there is an inverse monotonic dependence of the light charged particle multiplicity on impact parameter [16]. Although this is a plausible expectation for peripheral collisions where the energy deposition is changing rapidly with impact parameter, its validity for more central impact parameters is not well established. We can test this sensitivity of the total LCP multiplicity using our evaporation residue coincident data. (The fission fragment coincident LCP multiplicities are lower due to termination of the charged particle evaporation after fission.) We sum the $p,d,t,^3$He and ^{4}He multiplicities to get the total LCP multiplicity. At 25A MeV this total LCP multiplicity changes by less than 5% over the range where the mean impact parameter changes by a factor of two. At 35A MeV the mean impact parameter of our tags for different targets differs less, but again the multiplicities are the same within 5%. Thus total light charged particle multiplicities are not sensitive to the impact parameter in the fusionlike domain of impact parameter for the energies and projectile masses studied in this paper. In [17] Tsang *et al.* have used the Boltzmann equation to calculate the total nucleon multiplicity and find that for light projectiles such as ^{16}O there is no dependence on impact parameter for impact parameters less than about 5 fm. For larger impact parameters and energies higher than 35A MeV they do find that the total nucleon multiplicity depends on impact parameter.

C. Comparison of preequilibrium data to models

1. Comparison of preequilibrium proton spectra with a Fermi jet model

In this section we compare our data with a nucleon transport model [18] which has been quite successful in accounting for multiplicities and energy spectra of preequilibrium neutrons and protons in the 10 to 40 MeV bombarding energy domain. Briefly, the particle-target interactions are followed along classical trajectories. As a neck develops between the reactants nucleons are exchanged and the resulting one-body dissipation damps the kinetic energy of relative motion into internal thermal excitation energy. For purposes of calculating the preequilibrium emission at each time step along the trajectory the flux of transferred particles is sampled and individual nucleons are propagated through the receptor nucleus. Nucleon-nucleon collisions occur on a random basis depending on the nucleon-nucleon cross section. If scattering occurs before a particular nucleon reaches the nuclear surface, both the original and scattered nuclei are propagated until either they reach the surface and are emitted or until they are degraded in energy below the energy required to escape. After escape the particle energies are boosted to the laboratory frame and sorted into energy and angle bins. The calculations presented here are calculated as described in [19] and there was no parameter adjustment.

Calculations for both impact parameter ranges associated with evaporation residue and fission fragment tags are shown for the 25A MeV ^{16}O on Ta in Fig. 6 and for the 35A MeV data in Fig. 7. The model distinguishes the contributions from nucleons originating in the projectile (which dominate the forward angle spectra) and the nucleons which originate in the target (which dominate the backward angle spectra). The model provides an excellent account of both the magnitude and the spectral shape at forward angles. At the most backward angles however the calculation predicts too many particles originating from the target and propagated back through the projectile. The reason for this discrepancy is not understood. There are few previous studies where spectra have been measured over as complete an angular range as in this study so this aspect of backward emission has not been sufficiently tested. It is made more difficult because the thermal and preequilibrium components largely overlap in energy at the backward angles. The model does not address the thermal contribution. There is also a problem with the model calculations at backward angles in correcting for the spurious emission associated with the approximate treatment of the diffuse momentum distribution [19]. The subtraction of the contribution of spurious off-energy-shell emission can lead

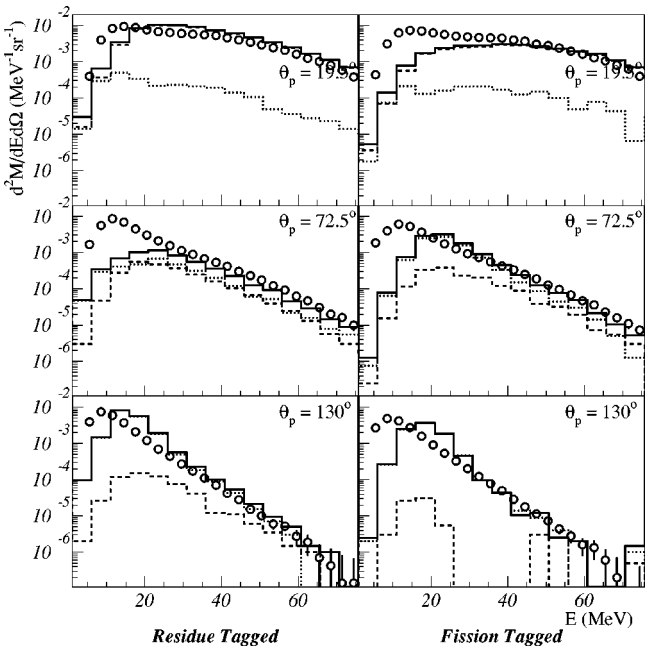

FIG. 6. Fermi jet calculation for the 25*A* MeV ^{16}O on Ta data. The three panels on the left are protons in coincidence with evaporation residues and the three panels on the right are protons in coincidence with fission fragments. The data are the open circles. The dashed histogram shows the contributions from nucleons originating in the projectile, the dotted histogram shows the nucleons which originate in the target, and the solid histogram is the sum of these contributions.

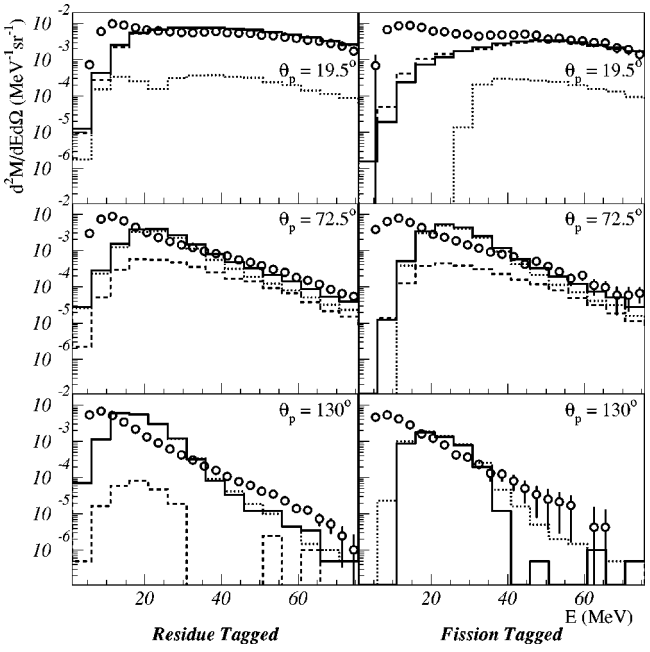

FIG. 7. Fermi jet calculation for the 35*A* MeV ^{14}N on Sm data. The three panels on the left are protons in coincidence with evaporation residues and the three panels on the right are protons in coincidence with fission fragments. The data are the open circles. The dashed histogram shows the contributions from nucleons originating in the projectile, the dotted histogram shows the nucleons which originate in the target, and the solid histogram is the sum of these contributions.

to negative probabilities for some angles and energies for particles originating in the projectile and appearing at back angles. This is responsible for the target contribution being larger than the total in the sixth panel of Fig. 7. Nevertheless the excellent agreement with the forward angle spectra where most of the energetic preequilibrium particles appear is gratifying. The impact parameter dependence of the total multiplicity for the preequilibrium protons originating in the projectile are compared with the data in Fig. 5, panel (a). The trends are reproduced but the absolute multiplicities are underpredicted, presumably due to emission of particles initiated by transfer from the target to the projectile.

2. Comparison of p, d, and t multiplicities with a transport model incorporating complex particle formation

The description of cluster formation and propagation in nuclear matter is a much more challenging problem than that of free nucleons. Danielewicz and Bertsch [1] have developed a model for deuteron formation based on the inverse of deuteron breakup induced by collision with a nucleon. Thus this corresponds to a three-nucleon interaction where two of the nucleons bind to form a deuteron and the third nucleon conserves energy and momentum. This approach has been extended to tritons by Danielewicz and Pan [2]. Triton formation is modeled as a four-nucleon process, but with the strength adjusted in such a way as to include contributions of breakup into deuterons as well as the inverse process. These processes have been incorporated into a transport model based on the Boltzmann-Uehling-Uhlenbeck (BUU) equation.

We have used this code to calculate the proton, deuteron, and triton production for some of our data samples. For consistency with our Fermi jet model calculations we have used nucleon-nucleon cross sections one half of the free nucleon-nucleon cross sections. The spectra produced with this modification are barely discernible from spectra produced with the full nucleon-nucleon cross sections. Otherwise there are no free parameters in this calculation. For our 25*A* MeV ^{16}O on Ta data we used an impact parameter of 2.3 fm to compare with our evaporation residue coincident sample and an impact parameter of 6.1 fm to compare with our fission fragment coincident sample. For our 35*A* MeV ^{14}N on Sm data we used impact parameters of 4.2 and 6.3 fm to compare with our evaporation residue and fission fragment tagged samples. We show samples of the calculations superposed on our proton, deuteron and triton data in Figs. 8 and 9.

The BUU calculations give a multiplicity roughly twice that of our data. This is particularly obvious at back angles and at low energies for all angles. The calculations were given enough time steps that they include production of evaporative particles from the compound nucleus and this low energy evaporative part seems to be primarily responsible for the large multiplicities. The high energy particle production at forward angles does have an impact parameter dependence. The calculation seems to have a larger impact parameter dependence than the data shows.

The back-angle discrepancy is reminiscent of the excess of back-angle yields in the Fermi jet model for transfers originating in the target and propagating back through the projectile.

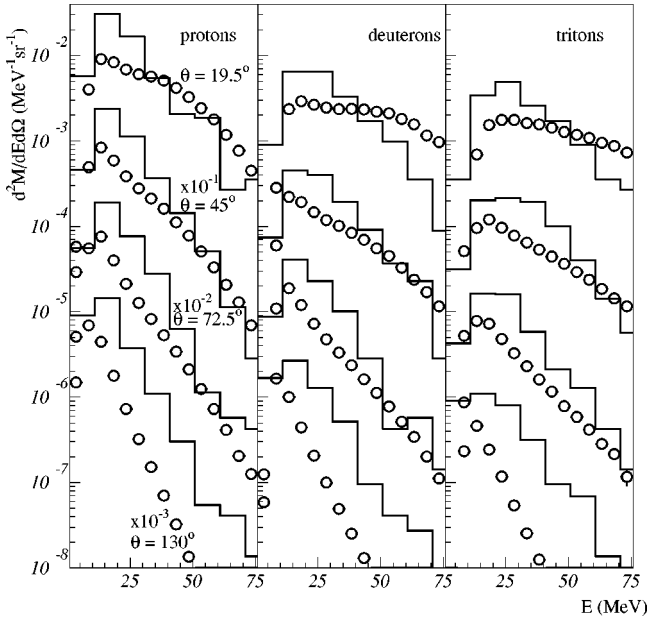

FIG. 8. BUU calculations for the 25*A* MeV ^{16}O on Ta evaporation residue coincident $Z=1$ data. The data are the open circles. The histograms are BUU calculations binned into 10 MeV wide bins. These calculations assume an impact parameter of 2.3 fm.

Although the calculated energy spectra exhibit more thermalization than the data, and the absolute multiplicities are overpredicted, the calculated d/p and t/p ratios are in quite good agreement with experiment considering the complexity of the calculation and the absence of adjustable parameters. This is demonstrated in Fig. 10 where we compare the calculated d/p and t/p ratios with the experimental values. The latter values are taken from Tables II and III and correspond to the total multiplicities including the equilibrium component, as the calculation follows the cascade long enough to include most of the equilibrium emission. The calculated values are for single impact parameters corresponding to the mean impact parameter of the tagged data. This is reasonable in that the calculation indicates a very weak dependence on impact parameter in the region explored.

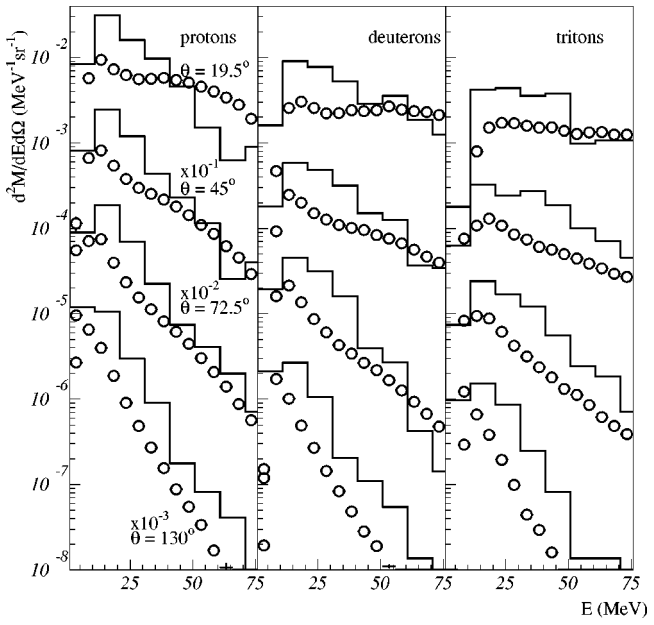

FIG. 9. BUU calculations for the 35*A* MeV ^{14}N on Sm evaporation residue coincident $Z=1$ data. The data are the open circles. The histograms are BUU calculations in 10 MeV wide bins. These calculations assume an impact parameter of 4.2 fm.

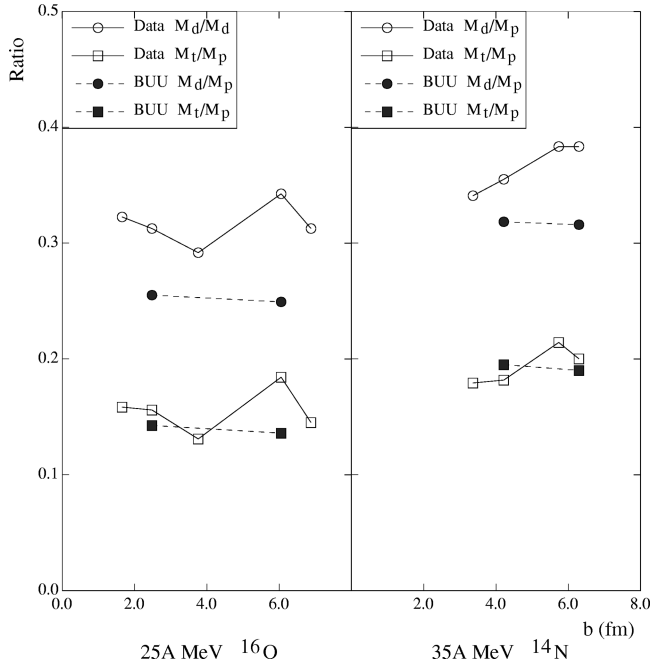

FIG. 10. Ratios of deuteron and triton total multiplicity to proton total multiplicity as a function of impact parameter. The data points (open symbols) are plotted at the mean impact parameters and connected by solid lines. The data are from Tables II and III and the impact parameters from Table I. The BUU calculations (solid symbols) are performed for the two impact parameters and connected by dashed lines.

IV. SUMMARY

The dependence of the energy spectra and multiplicities of light charged particles on impact parameter within the fusionlike impact parameter range have been determined at 25*A* MeV and 35*A* MeV bombarding energy. The energy spectra and their dependence on angle can be reasonably accounted for by assuming contributions from three sources, one with a velocity near the beam velocity, one with an intermediate velocity, and one with the velocity of an equilibrated source following incomplete fusion. Particular attention has been focused on the summed contributions of the first two sources, associated with preequilibrium emission. A nucleon exchange model (Fermi jet model) calculation for nucleons originating in the projectile accounts reasonably well for the forward and intermediate angle spectra. Inclusion of nucleons originating in the target leads to an overprediction at backward angles. The preequilibrium proton multiplicities fall off more slowly with increasing impact parameter than observed in a previous study at 14*A* MeV. The preequilibrium d/p and t/p ratios also vary more slowly with impact parameter than at the lower energy. These d/p and t/p ratios appear to have reached saturation values of about 0.5 and 0.3 by 25*A* MeV and do not increase at 35*A* MeV, whereas they were somewhat lower at 14*A* MeV.

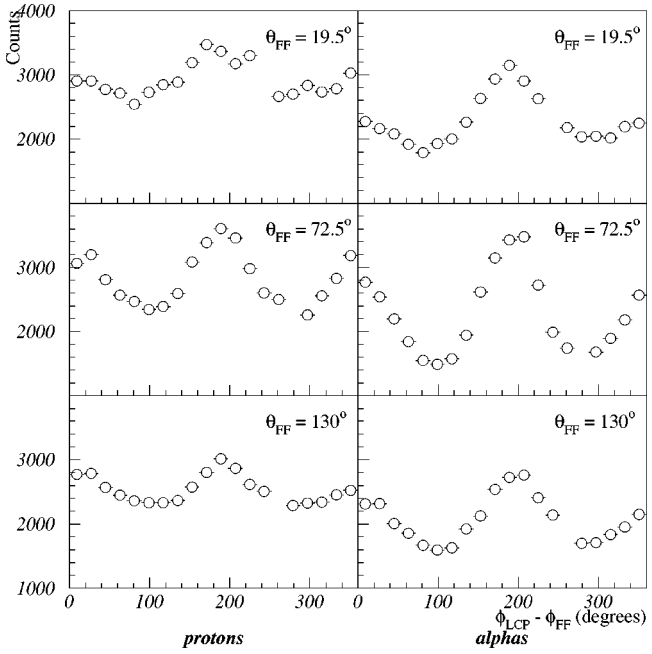

FIG. 11. Proton and alpha ϕ distributions as a function of detected fission fragment angle for the 25A MeV ^{16}O on ^{181}Ta data. The protons and alphas are detected at 57.5° from the beam. The fission fragments were detected at the angles listed in each panel. The zero has been suppressed to emphasize the dependence on the fission fragment angle.

A BUU transport model incorporating cluster formation based on the inverse of collision-induced breakup has been compared with the data. The model predicts more thermalization and higher absolute multiplicities than observed, but does a reasonable job of accounting for the d/p and t/p ratios and their dependence on impact parameter.

ACKNOWLEDGMENTS

This work was supported in part by the U.S. Department of Energy and the National Science Foundation.

APPENDIX A: TAG-LIGHT CHARGED PARTICLE KINEMATIC CORRELATIONS

1. Fission fragment-light charged particle correlations

One manifestation of the compound nucleus spin is the $W(180°)/W(90°)$ fission anisotropy. The spin of the compound nucleus is always perpendicular to the beam direction (neglecting preequilibrium emission) and the fission fragments are emitted preferentially perpendicular to the spin direction. Averaging over compound nucleus spin directions there is more opportunity for the fission fragment to be emitted at an angle of 0° or 180° than at 90° from the beam direction. The width of the fission fragment distribution relative to the spin direction is typically around 25°, so as the fission fragment is measured closer to the beam the determination of the spin direction gets worse.

The LCPs are also preferentially emitted perpendicular to the compound nucleus spin, in the same plane as the fission fragments. We demonstrate this in Fig. 11. In this figure we show the $\phi_{\mathrm{LCP}}-\phi_{\mathrm{FF}}$ dependence of LCPs detected at $\theta=57.5°$ in coincidence with fission fragments detected in selected ion chambers. The α particles have a stronger ϕ dependence than the protons and the fission fragment-LCP correlation is strongest when $\theta_{\mathrm{FF}}\approx 70°$. We also find that the higher energy LCPs have a stronger correlation with the fission fragment plane, as previously observed [20].

A close look at Fig. 11 shows that there are more α particles at 180° in ϕ away from the detected fission fragment than in the direction of the fission fragment. This is a kinematic effect due to the recoil of the compound nucleus from the emitted α particle. In [21] Wilson *et al.* see a similar kinematic effect. They use the LCPs to determine the reaction plane and to deduce the target and projectile sides. They see an enhancement of LCPs away from the projectile side, similar to our enhancement away from the side on which the fission fragment was detected. It is worth noting that when doing coincidence measurements the kinematic correlations can be surprisingly strong.

Since the ion chamber detectors are distributed throughout ϕ we could ignore the fission fragment-LCP ϕ correlations and still get a reasonable fit to a moving source parametrization. The primary concern is that the $W(180°)/W(90°)$ anisotropy of the α particles will cause a more forward peaking of the α particle distribution and result in an anomalously large preequilibrium multiplicity. Our solution is to include the fission fragment-LCP dependence in the moving source parametrization. We parameterize the fission fragment-LCP correlations in the data, then apply this parameterization to the moving source calculation during the χ^2 minimization.

We expect the ϕ dependence of the LCPs to be [22]

$$\exp[-\beta\,\sin^2(\phi_{\mathrm{LCP}}-\phi_{\mathrm{FF}})], \tag{A1}$$

where ϕ_{FF} is the azimuthal angle of the detected fission fragment. We expect β to depend on the polar angles of the fission fragment and LCP and the LCP energy as well as having a weak dependence on target. Binning the LCPs according to energy and θ and fitting each bin for each fission fragment tag according to Eq. (A1) we find that our data are well described by

$$\beta=0.004\,\sin(\theta_{\mathrm{LCP}})\sin(\theta_{\mathrm{FF}}^{\mathrm{CM}})E_{\mathrm{LCP}}. \tag{A2}$$

The constant 0.004 was extracted for the 25A MeV ^{16}O on Ta data. We expect a weak dependence on target and beam since the fission fragment anisotropies have this dependence. However including this correlation in the moving source fits turns out to have a small effect on the parameters so we use Eq. (A2) for all our fission fragment coincident data fits.

2. Evaporation residue-light charged particle kinematic correlations

Since the initial linear momentum is along the beam direction, the only way a residue will be observed in this experiment is through recoil from particle emission and or multiple Coulomb scattering. For the evaporation residues and target thicknesses in this experiment we expect the rms scattering angle to be around 6°. Since most of the evaporation residue detectors were at 7° and 11° recoil from particle emission is important. We demonstrate this in Fig. 12 where

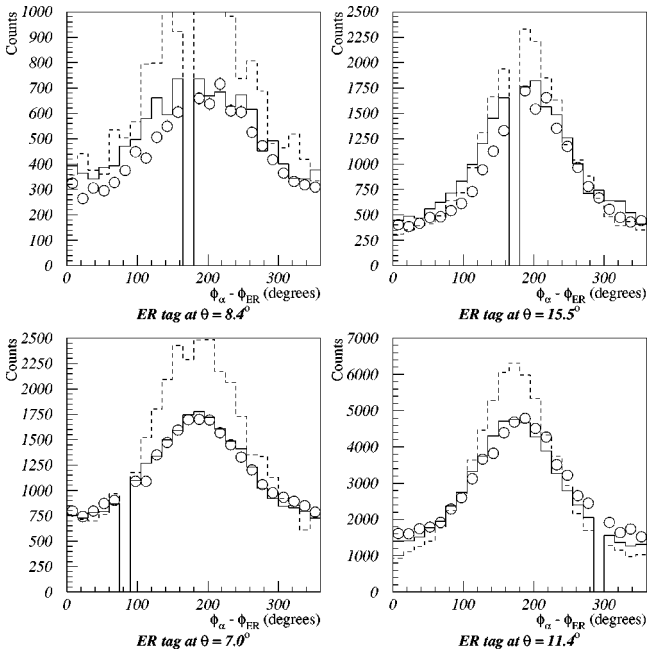

FIG. 12. ϕ distribution of α particles detected at $\theta = 35°$ in coincidence with evaporation residues. The evaporation residues were detected at the angles listed under each panel. The open circles are α particles in coincidence with evaporation residues from the 25*A* MeV ^{16}O on Ta data sample. The solid histogram is from a Monte-Carlo sample which used the LCP parameters extracted from moving source fits to the data. The dashed histogram is from a Monte-Carlo calculation in which we have arbitrarily reduced all multiplicities by a factor of two.

we plot the ϕ distribution of α particles in coincidence with an evaporation residue from the Ta data.

This correlation implies that the evaporation residue and LCP detection efficiencies are not independent. Schematically, we determine the multiplicity as

$$M = \frac{N_{\text{ER-LCP}}/\epsilon_{\text{LCP}}}{N_{\text{ER}}}. \tag{A3}$$

$N_{\text{ER-LCP}}$ is the number of LCPs observed in coincidence with an evaporation residue. As long as ϵ_{LCP} depends only on solid angle coverage and energy thresholds it is calculated implicitly by the moving source fit. N_{ER} is the number of events, and the difficulty is that the evaporation residue detection probability depends on the emitted LCPs. For certain angles and energies of LCP emission the recoil can be directly toward a residue detector giving a greatly enhanced efficiency for tagging that event. We take this into account by correcting N_{ER} by

$$\langle \epsilon_{\text{ER}} \rangle / \epsilon_{\text{ER(LCP)}}, \tag{A4}$$

where $\langle \epsilon_{\text{ER}} \rangle$ is the average evaporation residue detection efficiency and ϵ_{ER}(LCP), the correlated efficiency, reflecting the improved knowledge of the evaporation residue detection efficiency by virtue of having detected the particular LCP.

We calculate this ratio of efficiencies using Monte-Carlo techniques. For each Monte-Carlo event we generate a set of LCPs distributed according to a set of moving source parameters. We generate the projectilelike LCPs first, followed by prompt LCPs, then equilibrium LCPs. In addition to the LCPs we include neutron evaporation from the compound nucleus by assuming a multiplicity of 15 and the same temperature and source velocity as the evaporated protons. After LCP emission from each source we update the compound nucleus assuming mass and momentum conservation. The evaporation residue then undergoes multiple Coulomb scattering in the target. For each of the LCPs in the event we calculate the recoil direction. The difference between the recoil direction and the Monte-Carlo evaporation residue direction is a sample of the evaporation residue angular distribution, which we histogram and parameterize.

We calculate the recoil direction from each of the LCPs assuming momentum conservation. In order to center the recoil direction on the Monte-Carlo evaporation residue direction we need to assume 85% linear momentum transfer for the 25*A* MeV Monte-Carlo and 80% for the 35*A* MeV Monte-Carlo. In other words the LCPs carry away approximately 15% of the beam momentum for the 25*A* MeV ^{16}O data and 20% of the beam momentum for the 35*A* MeV ^{14}N data.

If the evaporation residue enters a residue detector we count this event as detected. The average evaporation residue efficiency, $\langle \epsilon_{\text{ER}} \rangle$, is the fraction of Monte-Carlo events that are detected. The coincidence efficiency, ϵ_{ER}(LCP), is the fraction of the evaporation residue recoil distribution that is covered by residue detectors. In the moving source fits (described in Sec. III B) we bin each LCP species in θ, ϕ, and energy. We correct the number of counts in each of these bins by the ratio $\epsilon_{\text{ER}}(\text{LCP})/\langle \epsilon_{\text{ER}} \rangle$, thereby normalizing to the average evaporation residue detection efficiency.

We verify this procedure is reasonable by fitting the Monte-Carlo event samples and extracting parameters close to the values of the parameters used to generate the sample.

In Fig. 12 we explore the evaporation residue-LCP correlation dependence on the LCP distributions. We have extracted source parameters from the data (using the multisource fit) and generated Monte Carlo events with the LCPs distributed according to these parameters. The solid line in Fig. 12 shows the LCP ϕ distributions for selected evaporation residue tags, and we observe that the Monte-Carlo is very similar to the data. We generate a second Monte Carlo data set using the same parameters except for the multiplicities, which we arbitrarily reduce by a factor of two. These α particle distributions, shown by the dotted curve, are noticeably narrower. This demonstrates that the width of the evaporation residue distributions depend on the LCP emission and we have some sensitivity to it.

APPENDIX B: MOVING SOURCE FIT DETAILS

In the source frame particle evaporation from a volume source has the form

$$\frac{d^2N}{dE\,d\Omega} = \frac{M_{\text{source}} N_{\text{tag}}}{2(\pi T_{\text{source}})^{3/2}} \sqrt{E - V_{\text{source}}} \times \exp[-(E - V_{\text{source}})/T_{\text{source}}] \tag{B1}$$

and evaporation from a surface has the form

$$\frac{d^2N}{dEd\Omega}=\frac{M_{\rm source}N_{\rm tag}}{4\pi T_{\rm source}^2}(E-V_{\rm source})\exp[-(E-V_{\rm source})/T_{\rm source}], \tag{B2}$$

where $N_{\rm tag}$ is the number of observed LCPs, $M_{\rm source}$ is the multiplicity, and $T_{\rm source}$ and $V_{\rm source}$ are the temperature and Coulomb barriers. The transformation from the source to laboratory frames is different if the Coulomb barrier is considered to be in the source frame or the laboratory frame. For evaporation from the compound nucleus and fission fragments it makes sense to think of the Coulomb barrier in the source frame. These are both surface emission and their functional form is

$$\frac{d^2N}{dE_{\rm lab}d\Omega_{\rm lab}}=\frac{M_{\rm source}N_{\rm tag}}{4\pi T_{\rm source}^2}E''\sqrt{E_{\rm lab}/E'}\exp(-E''/T_{\rm source}). \tag{B3}$$

When the Coulomb barrier is in the source frame E' and E'' are defined as

$$E'=E_{\rm lab}-2\sqrt{E_{\rm lab}\frac{1}{2}m_{\rm LCP}v_{\rm source}^2}\cos(\theta)+\frac{1}{2}m_{\rm LCP}v_{\rm source}^2 \tag{B4}$$

and

$$E''=E'-V_{\rm source}. \tag{B5}$$

$v_{\rm source}$ is the magnitude of the source velocity and is taken along the beam direction for evaporation from the compound nucleus or the fission fragment direction for evaporation from the fragments. θ is the angle from the source direction to the detected LCP.

We think of the prompt and projectilelike source emission as occurring during the fusion process and before equilibration. The majority of the electric charge originates from the target and must be essentially at rest compared to the source velocities, so it makes sense to assume the Coulomb barrier is in the laboratory frame. In this case the prompt (volume) source has the form

$$\frac{d^2N}{dE_{\rm lab}d\Omega_{\rm lab}}=\frac{M_{\rm source}N_{\rm tag}}{2(\pi T_{\rm source})^{3/2}}\sqrt{E'}\exp(-E''/T_{\rm source}) \tag{B6}$$

and the projectile (surface) source has the form

$$\frac{d^2N}{dE_{\rm lab}d\Omega_{\rm lab}}=\frac{M_{\rm source}N_{\rm tag}}{4\pi T_{\rm source}^2}\sqrt{E'E''}\exp(-E''/T_{\rm source}). \tag{B7}$$

When the Coulomb barrier is in the laboratory frame E' and E'' are defined as

$$E'=E_{\rm lab}-V_{\rm source} \tag{B8}$$

and

$$E''=E'-2\sqrt{E'\frac{1}{2}m_{\rm LCP}v_{\rm source}^2}\cos(\theta)+\frac{1}{2}m_{\rm LCP}v_{\rm source}^2. \tag{B9}$$

In practice the Coulomb barriers of these sources is poorly determined by the data so we constrain them to be the same as the Coulomb barrier of the compound nucleus evaporative source which is well determined.

To determine the source parameters we minimize the χ^2

$$\chi^2=\sum_E\sum_{MB}\frac{[N_{\rm obs}(E,MB)-N_{\rm pred}(E,MB)]^2}{N_{\rm pred}(E,MB)}, \tag{B10}$$

where $N_{\rm obs}(E,MB)$ is the number of measured LCPs in miniball detector MB in the energy bin E. $N_{\rm pred}(E,MB)$ is the sum of the contributions from all the sources with a correction to account for correlations between the tag and the LCP detection. We also convolute $N_{\rm pred}(E,MB)$ by a Gaussian with $\sigma=2$ MeV. We do this because the different miniball counters have slightly different energy thresholds and this convolution smears the threshold effects enough that the fit is insensitive to the lower energy limit of the fit which we can set very low.

For the evaporation residue tag we have

$$N_{\rm pred}(E,MB)=\frac{\langle\epsilon_{\rm ER}\rangle}{\epsilon_{\rm ER}({\rm LCP})}\left[\left(\frac{d^2N}{dEd\Omega}\right)_{\rm projectile}+\left(\frac{d^2N}{dEd\Omega}\right)_{\rm prompt}+\left(\frac{d^2N}{dEd\Omega}\right)_{\rm CN}\right]\Delta E\Delta\Omega, \tag{B11}$$

where we use 1 MeV bins for ΔE and $\Delta\Omega$ is the solid angle of the particular miniball detector. The factor $\langle\epsilon_{\rm ER}\rangle/\epsilon_{\rm ER}({\rm LCP})$ corrects for the kinematic effect that the evaporation residue recoiling from this particular LCP has a different detection efficiency than an ''average'' evaporation residue and this is calculated using Monte-Carlo techniques as described in Sec. A 2. This efficiency correction has a small effect on all parameters except for the prompt and projectilelike sources of the triton and alpha multiplicities. As mentioned previously, we fix the projectilelike and prompt sources to have the same Coulomb barrier as the compound nucleus source, and we fix the projectilelike source velocity to be 90% of the beam velocity. Thus we have a total of nine parameters to fit the energy, θ and ϕ dependence of each LCP type.

For the fission fragment coincident data we include fission fragment sources so we have

$$N_{\rm pred}(E,MB)=\left\{\sum_{\rm IC}(\exp[-0.004E\,\sin^2(\phi-\phi_{\rm FF})])\times\left[A_1\left(\frac{d^2N}{dEd\Omega}\right)_{\rm projectile}+A_2\left(\frac{d^2N}{dEd\Omega}\right)_{\rm prompt}+A_3\left(\frac{d^2N}{dEd\Omega}\right)_{CN}\right]+\sum_{\rm IC}\left(\frac{d^2N}{dEd\Omega}\right)_{\rm FF}\right\}\Delta E\Delta\Omega, \tag{B12}$$

where A_1, A_2, and A_3 are normalization constants needed because of the ϕ dependent factor. There are ten ion chamber detectors and with their complementary fragments, a to-

tal of 20 fission fragment sources. We treat all these fission fragment sources identically except for the normalization being the number of fission fragments actually detected in that ion chamber and the source velocity being along the ion chamber counter direction and the expected complementary angle. Additionally we fix the source velocity at $1A$ MeV in the compound nucleus frame. Thus we introduce only another three parameters, the temperature, multiplicity and Coulomb barrier.

Without the kinematic correlation corrections one can explicitly integrate the moving source equations and verify that the parameter M_{source} is the number of LCPs per tag. The ratio of efficiencies, $\langle \epsilon_{\text{ER}} \rangle / \epsilon_{\text{ER}}(\text{LCP})$, introduced for the evaporation residue coincident data is a correction to the number of evaporation residue tags, so although it depends on the LCPs it should be kept outside of the energy and angle integrations. On the other hand the inclusion of the ϕ correlations, $\Sigma_{\text{IC}} \exp[-0.004E \sin^2(\phi - \phi_{\text{FF}})]$, for the fission fragment coincident data would cause the moving source equations to not be normalized without the inclusion of A_1, A_2, and A_3. We numerically integrate to determine these constants. Because the ion chamber counters are nearly uniformly distributed in ϕ this correction turns out to be small in practice.

[1] P. Danielewicz and G. F. Bertsch, Nucl. Phys. **A553**, 712 (1991).

[2] P. Danielewicz and Quibao Pan, Phys. Rev. C **46**, 2002 (1992).

[3] D. Prindle, R. Vandenbosch, S. Kailas, A. Charlop, and C. Hyde-Wright, Phys. Rev. C **48**, 291 (1993).

[4] R. T. de Souza, N. Carlin, Y. D. Kim, J. Ottarson, L. Phair, D. R. Bowman, C. K. Gelbke, W. G. Gong, W. G. Lynch, R. A. Pelak, T. Peterson, G. Poggi, M. B. Tsang, and H. M. Xu, Nucl. Instrum. Methods Phys. Res. A **295**, 109 (1990).

[5] D. Fox, R. T. de Souza, S. L. Chen, B. Davin, T. M. Hamilton, J. Dorsett, and J. Ottarson, Nucl. Instrum. Methods Phys. Res. A **368**, 709 (1996).

[6] A. A. Sonzogni, A. Elmaani, C. Hyde-Wright, W. Jiang, D. Prindle, R. Vandenbosch, J. Dinius, G. Cron, C. K. Gelbke, W. Hsi, W. G. Lynch, C. Montoya, G. Peaslee, R. T. de Souza, D. Fox, and T. Moore, Phys. Rev. C **53**, 243 (1995).

[7] S. Y. van der Werf, Nucl. Instrum. Methods **153**, 221 (1978).

[8] M. B. Tsang and P. Danielewicz, MSUCL-1069 (1997).

[9] W. E. Parker, M. Kaplan, D. J. Moses, J. M. Alexander, J. T. Boger, R. A. Lacey, and D. M. de Castro Rizzo, Nucl. Phys. **A568**, 633 (1994).

[10] C. J. Gelderloos, R. Sun, N. N. Ajitanand, J. M. Alexander, E. Bauge, A. Elmaani, T. Ethvignot, R. A. Lacey, M. E. Brandon, A. Giorni, D. Heuer, S. Kox, A. Lleres, A. Menchaca-Rocha, F. Merchez, D. Rebreyend, J. B. Viano, B. Chambon, B. Cheynis, D. Drain, and C. Pastor, Phys. Rev. C **52**, R2834 (1995).

[11] T. C. Awes, G. Poggi, C. K. Gelbke, B. B. Black, B. G. Glagola, H. Breuer, and V. E. Viola, Phys. Rev. C **24**, 89 (1981).

[12] R. Wada, D. Fabris, K. Hagel, G. Nebbia, Y. Lou, M. Gonin, J. B. Natowitz, R. Billerey, B. Cheynis, A. Demeyer, D. Guinet, C. Pastor, L. Vagneron, K. Zaid, J. Alarja, A. Giorni, D. Heuer, C. Morand, B. Viano, C. Mazur, C. Ngô, S. Leray, R. Lucas, M. Ribrag, and E. Tomasi, Phys. Rev. C **39**, 497 (1989).

[13] D. J. Fields, W. G. Lynch, T. K. Nayak, M. B. Tsang, C. B. Chitwood, C. K. Gelbke, R. Morse, J. Wilczynski, T. C. Awes, R. L. Ferguson, F. Plasil, F. E. Obenshain, and G. R. Young, Phys. Rev. C **34**, 536 (1986).

[14] F. Benrachi, B. Chambon, B. Cheynis, D. Drain, C. Pastor, H. Rossner, D. Hilscher, B. Gebauer, D. Husson, A. Giorni, D. Heuer, A. Lleres, P. Stassi, and J. B. Viano, Phys. Rev. C **48**, 2340 (1993).

[15] D. Sackett, A. Galonsky, C. K. Gelbke, H. Hama, L. Heilbronn, D. Krofcheck, W. G. Lynch, H. R. Schelin, M. B. Tsang, X. Yang, F. Deák, Á. Horváth, Á. Kiss, Z. Seres, J. Kasagi, and T. Murakami, Phys. Rev. C **44**, 384 (1991).

[16] A. Del Zoppo, R. Alba, C. Agodi, G. Bellia, R. Coniglione, P. Finocchiaro, V. Latora, K. Loukachine, C. Maiolino, E. Migneco, A. Peghaire, P. Piattelli, D. Santonocito, and P. Sapienza, Phys. Rev. C **50**, 2930 (1994).

[17] M. B. Tsang, G. F. Bertsch, W. G. Lynch, and M. Tohyama, Phys. Rev. C **40**, 1685 (1989).

[18] J. Randrup and R. Vandenbosch, Nucl. Phys. **A474**, 219 (1987).

[19] S. J. Luke, R. Vandenbosch, and J. Randrup, Phys. Rev. C **48**, 857 (1993).

[20] M. B. Tsang, Y. D. Carlin, Z. Chen, C. K. Gelbke, W. G. Gong, W. G. Lynch, T. Murakami, T. Nayak, R. M. Ronnigen, H. M. Xu, F. Zhu, L. G. Sobotka, D. W. Stracener, D. G. Sarantites, Z. Majka, and V. Abenante, Phys. Rev. C **42**, R15 (1990).

[21] W. K. Wilson, W. Benenson, D. A. Cebra, J. Clayton, S. Howden, J. Karn, T. Li, C. A. Ogilvie, A. Vander Molen, G. D. Westfall, J. S. Winfield, B. Young, and A. Nadasen, Phys. Rev. C **41**, R1881 (1990).

[22] M. B. Tsang, C. B. Chitwood, D. J. Fields, C. K. Gelbke, D. R. Klesch, W. G. Lynch, K. Kwiatkowski, and V. E. Viola, Phys. Rev. Lett. **52**, 1967 (1984).